

SIMULATION OF MAGNETOHYDRODYNAMIC FLOWS: A CONSTRAINED TRANSPORT METHOD

CHARLES R. EVANS

Theoretical Astrophysics, California Institute of Technology

AND

JOHN F. HAWLEY

Theoretical Astrophysics, California Institute of Technology; and Department of Astronomy, University of Virginia

Received 1987 November 23; accepted 1988 March 9

ABSTRACT

We discuss an optimal strategy for treating the magnetohydrodynamic (MHD) field transport (induction) equation. The induction equation is shown to assume its simplest form when written in terms of the contravariant forms of velocity and magnetic vector density. The approach places the induction equation in integral form and uses the magnetic flux as a fundamental variable. We describe a new numerical technique, called constrained transport (CT), for evolving the induction equation in a way that maintains vanishing divergence of the poloidal (constrained) field components to within machine round-off error. The scheme places no restrictions on the order of accuracy of the transport technique and is shown to work in three dimensions as well as in two. We show that CT allows incorporation of an adaptive mesh algorithm in a natural way. No barrier is evident to prevent the use of the technique in nonideal MHD simulations. Some past treatments of the MHD induction equation are reviewed, with attention to the question of constraint satisfaction. We show how the $3 + 1$ formalism of numerical relativity can be used to express the general relativistic MHD equations in a form suitable for numerical evolution. The relativistic form of the magnetic induction equation is then shown to fit naturally within the CT scheme. An axisymmetric, two-dimensional finite-difference code has been constructed incorporating the new method for the induction equation. Results obtained using the CT method are compared with those obtained from a code employing vector potential evolution. Several models involving magnetized flow near a black hole are used as calibrations of the CT scheme.

Subject headings: black holes — galaxies: nuclei — hydromagnetics

I. INTRODUCTION

The desirability of performing global magnetohydrodynamic (MHD) simulations in astrophysics hardly needs repeating. There are few areas of astrophysical theory where magnetic fields are not on occasion invoked to explain observed phenomena. For some astrophysical processes magnetic fields are believed to be of critical importance, e.g., magnetic braking of protostellar clouds, MHD shocks, magnetospheres, neutron star and magnetic white dwarf accretion columns. Yet these equations are of such complexity that solutions can usually be obtained only through numerical techniques.

The astrophysical literature contains many examples of numerical global MHD simulations. Two of the most active areas of research have been studies of the dynamics of the solar wind and the Earth's magnetosphere (reviewed by Brecht 1985), and modeling of protostellar, self-gravitating clouds (Dorfi 1986). Recently, interest in MHD has been stimulated by the study of radio jets and active galaxies. It is probable that magnetic fields are fundamental in a jet's generation, acceleration, and collimation. For example, magnetized winds centrifugally driven off an accretion disk have been suggested as a source of mass flux for jets (Blandford and Payne 1982). The subsequent collimation of the jet may be created and maintained by a toroidal magnetic field that provides an axis-directed tension force (see, for example, Chan and Hendriksen 1980; Benford 1981; Achterberg, Blandford, and Goldreich 1983; Clarke, Norman, and Burns 1986). In preliminary investigations, Clarke, Norman, and Burns (1986) and Lind, Blandford, Payne, and Meier (Lind 1986) have evolved axisymmetric gas jets with both passive and active toroidal fields. Norman, Clarke, and Burns (1987) have since extended their work to include an active poloidal field. The complexity uncovered by even these highly idealized simulations forcefully demonstrates that although we are well aware of the *importance* of magnetic fields in astrophysics, we do not have a commensurate theoretical *understanding* of MHD processes.

In this paper we begin developing and documenting a general relativistic MHD code. We are motivated by the need to investigate MHD processes in active galaxies, radio jets, and the black holes believed to power them. A study of general relativistic MHD effects in accretion flows is a natural extension of previous work on relativistic hydrodynamics near central engines (Hawley, Smarr, and Wilson 1984*a, b*; hereafter HSW*a, b*). Black hole MHD is one area where uniquely general relativistic effects play an important and direct role in observable phenomena. For example, Blandford and Znajek (1977) have shown that energy and angular momentum can be extracted from a rotating black hole by an accretion-induced magnetic field threading the hole's horizon. This electromagnetic extraction arises through the action of the Kerr hole's "gravitomagnetic potential" β^i (the shift vector; see MacDonald and Thorne 1982; also Thorne, Price, and MacDonald 1986).

A fully relativistic treatment of the MHD equations is required to model the hydromagnetic flow right down to the black hole, thus treating the innermost region of an AGN, and to calculate a relativistic MHD outflow, or wind. Nonetheless, the main result of

this paper, the numerical treatment of the magnetic transport (induction) equation, has a much broader applicability to more typical Newtonian MHD calculations.

The principal concerns of this paper are (1) placement of the general relativistic MHD equations in a form most suitable for numerical treatment, (2) derivation of a numerical scheme for the induction equation, and (3) calculation of a set of hydromagnetic flows as calibrations of the transport scheme. While the numerical treatment of the Newtonian part of the Lorentz force is fairly straightforward, differencing the uniquely relativistic terms (e.g., the displacement current and charge separation terms) is not, so the entire discussion of the Lorentz force is left to a later paper.

The outline of this paper is as follows. In § II we briefly discuss the Newtonian magnetic induction equation and how it can be placed in the very simple form that is crucial to the finite-difference method we develop. We then place the general relativistic 3 + 1 induction equation in an analogous form. Some details of the 3 + 1 formalism and the derivation of the induction equation are given in an Appendix. In § IIc we discuss the integral form of the induction equation, essential to the development of the numerical scheme. Section III briefly reviews the numerical issues associated with MHD field transport, particularly the problem of magnetic constraint violation. Section IV describes a new numerical approach, called *constrained transport* (CT), to evolve the induction equation while maintaining vanishing divergence of the magnetic field down to machine round-off error. Constrained transport is sufficiently general that it (1) works in arbitrary coordinate systems, (2) places no restrictions on the order of accuracy of the transport technique employed, (3) works in three dimensions as well as in two, (4) allows incorporation of an adaptive mesh algorithm, and (5) presents no barrier to its use in nonideal MHD simulations. Finally, numerical tests of the scheme are discussed in § V using a two dimensional finite-difference code. Two separate testing programs are carried out. First, simple advection of a magnetic field on a Newtonian, Cartesian mesh provides a graphic demonstration of the main advantages of the CT scheme. Next, several problems involving hydromagnetic flows onto a black hole provide calibration in the context of the problem of interest, viz., central engines. In each case the results are contrasted with those obtained with a vector potential approach.

II. MAGNETIC FIELD TRANSPORT IN MHD

a) Newtonian Magnetic Field Transport

We begin with a brief discussion of the *Newtonian* magnetic induction equation. The ideal MHD induction equation, written in its usual vector notation form, is

$$\partial_t \mathbf{B} = \nabla \times (\mathbf{V} \times \mathbf{B}). \quad (2.1)$$

Since our aim is to solve (2.1) numerically, it must be written in component form,

$$\partial_t B^i = \epsilon^{ijk} \nabla_j (\epsilon_{klm} V^l B^m), \quad (2.2)$$

where ∇_j is the covariant derivative. The curvilinear generalization of the curl and cross product make use the Levi-Civita tensor

$$\epsilon^{ijk} = \gamma^{-1/2} [ijk], \quad \epsilon_{ijk} = \gamma \epsilon^{ijk}. \quad (2.3)$$

Here γ is the determinant of the metric tensor in the chosen coordinate system and $[ijk]$ is the location-independent totally antisymmetric symbol (+1 for even permutations of i, j, k , -1 for odd permutations of i, j, k , and 0 otherwise).

It is then easy to show that equation (2.2) can be reduced to the particularly simple expression

$$\partial_t \mathcal{B}^i = \partial_j (V^j \mathcal{B}^i - V^i \mathcal{B}^j), \quad (2.4)$$

where now only the partial derivative ∂_j appears and where \mathcal{B}^i is the magnetic vector *density* defined by

$$\mathcal{B}^i \equiv \gamma^{1/2} B^i. \quad (2.5)$$

The constraint on the magnetic field has an equally concise form when written in terms of the magnetic vector density (2.5),

$$\partial_i \mathcal{B}^i = 0. \quad (2.6)$$

It should be noted that equations (2.4) and (2.6) have a Cartesian appearance even though they are valid for arbitrary curvilinear coordinates. The metric describing those coordinates never directly appears, although it is hidden in the definition (2.5) of \mathcal{B}^i . This nice result, which is crucial to the constraint-preserving numerical scheme we develop, requires the use of the contravariant forms (raised indices) of the velocity and the magnetic vector density. In numerous past calculations, *physical* components (physical in the sense of fluid dynamicists; i.e., orthonormal components) were used, which reintroduce the metric and make the induction equation more complex than equation (2.4).

b) General Relativistic Magnetic Field Transport

The convenient form given above for Newtonian MHD is mirrored in general relativity. To express general relativistic results we use the 3 + 1 formalism (see the Appendix for more details and citations). The 3 + 1 decomposition of the line element is

$$ds^2 = -\alpha^2 dt^2 + \gamma_{ij} (dx^i + \beta^i dt)(dx^j + \beta^j dt), \quad (2.7)$$

in terms of the lapse function α , shift vector β^i and spatial three-metric γ_{ij} . No restrictive assumptions about the nature of the background spacetime are made. For many applications we will be interested in specializing to a stationary background (e.g., to the non-self-gravitating flow near an AGN black hole), but the expressions given here are more general and cover cases when the spacetime is time dependent.

Using the usual definition (HSWa) of the transport velocity $V^i \equiv U^i/U^t$, the *general relativistic* magnetic induction equation has the form

$$\partial_t \mathcal{B}^i = \partial_j [(V^i - \beta^i) \mathcal{B}^j - (V^j - \beta^j) \mathcal{B}^i] . \quad (2.8)$$

When written this way the general relativistic induction equation has essentially the same form as its flat-space variant (2.4), differing only through the presence of the shift vector (the gravitomagnetic potential). Now, however, equation (2.8) represents the magnetic field transport in an arbitrarily curved, and dynamic spacetime with arbitrary choices for the spacetime coordinates, despite its “Cartesian” appearance. General relativity does not alter the form of the constraint on the field (2.6).

We see that field transport equations (2.4) and (2.8) analytically preserve the divergence constraint (2.6) during time evolution.

c) Integral Form and Kinematics

The most natural route to finite-differencing the MHD equations comes from placing the induction equation in integral form. There are two advantages to doing this. First, we find that the most appropriate quantity to be differenced is the magnetic flux Φ_S piercing a two-surface S . Second, it becomes obvious once the induction equation is in integral form how to incorporate an adaptive mesh into the numerical scheme.

The magnetic flux piercing a two-surface element S lying in a slice of constant coordinate time t is

$$\Phi_S = \int_S B^i d\Sigma_i , \quad (2.9)$$

where $d\Sigma_i$ is the spatially covariant area element. Now suppose that the magnetic field is time dependent and that the finite area element is as well, i.e., $S = S(t)$. Let V_g^i be defined as the coordinate velocity describing the flow of points within $S(t)$ from time slice to time slice. The region $S(t)$ has a contour $\partial S(t)$ as its boundary. Just as in flat spacetime, the total rate of change of the flux piercing this moving surface, $d\Phi_{S(t)}/dt$, equals minus the total electromotive force (EMF), \mathcal{E} , around the contour $\partial S(t)$. The partial time derivative ∂_t gives the change in a quantity per unit coordinate time along fixed spatial coordinate values x^i . The convective (or adaptive mesh) time derivative δ_t is defined as giving the change per unit coordinate time along points that are moving with velocity V_g^i . We then have, for example, the rate of change of the magnetic field along points moving with $S(t)$,

$$\delta_t B^i = \partial_t B^i + V_g^k \partial_k B^i . \quad (2.10)$$

In particular the convective velocity V_g^i (a “grid” velocity for a finite-difference scheme) is itself defined by

$$\delta_t x^i \equiv V_g^i . \quad (2.11)$$

With these definitions, the magnetic field transport equation (2.8) can be expressed in integral form (see the Appendix), using the magnetic vector density (2.5) and Stokes theorem,

$$\begin{aligned} \frac{d}{dt} \Phi_{S(t)} &= \frac{d}{dt} \int_{S(t)} B^i d\Sigma_i = \frac{d}{dt} \int_{S(t)} \mathcal{B}^i d\Sigma_i^{(c)} = -\mathcal{E} \\ &= \oint_{\partial S(t)} (V^i - V_g^i - \beta^i) B^j \epsilon_{ijk} dx^k = \oint_{\partial S(t)} (V^i - V_g^i - \beta^i) \mathcal{B}^j [ijk] dx^k . \end{aligned} \quad (2.12)$$

In equation (2.12) $d\Sigma_i^{(c)}$ is the coordinate area element, and \mathcal{E} is the EMF about the contour $\partial S(t)$ due to the combined effects of fluid motion, gravitomagnetic potential and motion of the circuit. Equation (2.12) can also be derived from equation (3.49) of Thorne *et al.* (1986; see also Thorne and MacDonald 1982) using the ideal MHD condition. The usual nonrelativistic result arises by simply setting the shift vector β^i to vanish.

In § IV, equation (2.12) becomes the basis of our constraint-preserving adaptive mesh numerical transport algorithm.

III. NUMERICAL PROBLEMS AND ISSUES

Although we are primarily concerned with general relativistic MHD, it is clear from the above discussion that the Newtonian and relativistic induction equations are quite similar. The numerical techniques used will have a corresponding familiarity, and in this section we review concerns and issues raised by previous numerical solutions of the magnetic induction equation.

The goal in a numerical evolution of the induction equation is to obtain accurate fields from which to calculate the Lorentz force. Those fields should be divergenceless, $\nabla \cdot \mathbf{B} = 0$. But this condition is an initial *constraint*, not an evolution equation, and while it is maintained analytically by the field evolution equations, it in general will not be by the finite-difference equations. A nonzero divergence in the magnetic field is a symptom of numerical error, and, as emphasized by Brackbill and Barnes (1980), this error can produce an anomalous force *parallel* to the magnetic field, especially when one uses the conservative form of the momentum equation. Brackbill and Barnes (1980) show that these errors are substantially reduced by differencing the momentum equation in nonconservative form (i.e., using the form $\mathbf{J} \times \mathbf{B}$ for the Lorentz force). With this modification, they obtain significantly improved test results with errors in kinetic energy reduced by a factor of 4000. Similar improvements in performance have been reported by Finan and Killeen (1981). We note, however, that while use of the nonconservative form of the momentum equation guards against development of a manifestly unphysical force parallel to the magnetic field, one must be concerned that a force term expressed as $\mathbf{J} \times \mathbf{B}$ nevertheless yields inaccurate results when the magnetic field cannot be trusted.

How then to improve on the trustworthiness of the magnetic field? The magnetic induction equation can be solved by evolving either the field components, or the vector potential. While these two approaches are analytically identical, they have separate

numerical advantages and disadvantages. The vector potential technique is often used for the stated reason that it insures maintenance of the magnetic field constraint. This will be true provided one's finite-difference representations of the divergence and curl operators combine to allow the discrete representation of $\nabla \cdot \nabla \times$ taken on any vector to vanish identically. In two-dimensional simulations it is sufficient to evolve a single scalar, namely, the vector potential component along the symmetry axis (e.g., A_ϕ). This approach was used by Wilson (1975) in his pioneering calculations of magnetic effects in black hole accretion. Lind (1986) and Clarke, Norman, and Burns (1986) have used this technique in two-dimensional cylindrical axisymmetric jet calculations. For the more general three-dimensional calculation, Dorfi (1986) developed constrained vector potential differencing schemes in specific coordinate systems (e.g., spherical-polar, cylindrical, Cartesian) by restricting the schemes to be first order. In § IV we extend this basic idea to arbitrary coordinate systems by adopting the covariant form of the vector potential induction equation and an appropriate centering of variables. Straightforward and accurate higher-order finite differencing can then provide numerical consistency between the poloidal field, generated by vector potential evolution, and the divergence constraint.

However, even for a fully constrained evolution there remains a serious problem with the vector potential approach. The Lorentz force $\mathbf{J} \times \mathbf{B} = (\nabla \times \mathbf{B}) \times \mathbf{B}/4\pi$ involves second derivatives of the vector potential, and these can be difficult to accurately model in a finite-difference calculation. This problem is most recently discussed by Norman, Clarke, and Burns (1987), who are concerned that for each successive difference taken of an initially second-order accurate discrete representation of a function ψ the order of accuracy is reduced by one in comparing the relevant spatial differences of ψ to its corresponding analytic derivative. In the present context this argument would suggest that if A is accurate up to a second-order truncation error $\epsilon = \mathcal{O}(h^2)$, where $h = \Delta x/l$ and l is the characteristic length scale for variation in A , then the Lorentz force would have a truncation error of order unity! These authors have recommended the use of a third-order method (such as the "piecewise parabolic method" of Colella and Woodward 1984).

This question of the relative order of accuracy of a numerically evolved variable and its derivatives has been summarized by Choptuik (1986), who gives a counterargument to the one above. Choptuik's point is based on what is known as Richardson's hypothesis. This holds that the truncation error in A , i.e., the difference between a discrete sampling of analytic values of A and corresponding values \tilde{A} obtained from a second-order finite-difference approximation, is a term of the form

$$A(x_i) - \tilde{A}_i = h^2 f(x_i), \quad (3.1)$$

where $f(x)$ is a *smooth* function of position that is *independent* of the mesh spacing. Provided the function $f(x)$ is well behaved (and this is dependent on the difference algorithm that generates \tilde{A}), the error in the finite-difference approximation of the second derivative is

$$A''(x_i) - \tilde{A}_i'' = h^2 [f''(x_i) + \mathcal{O}(h^2)]. \quad (3.2)$$

Hence the order of accuracy for a derivative remains the same as the original finite-difference approximation for A .

Thus, it is not so much the formal order of the vector potential scheme that is of concern as the effect on the force term produced by sudden changes in the characteristic length scale. With vector potential evolution the problem centers on anomalous current, or force, reversals in the vicinity of sharp features in the magnetic field (such as those associated with shocks). In a sharp numerical feature representing a discontinuity in the field, the characteristic length scale l approaches several zone widths and locally all schemes then have a truncation error of order unity. Many "smooth" finite-difference schemes respond to sharp features by throwing power into high wavenumber modes, and thereby producing "ringing." In a second difference these high wavenumber modes are even more pronounced. In hydrodynamics it has proved feasible to find monotonic or "flux-correcting" transport schemes (see discussion of several such schemes in HSWb, Woodward and Colella 1984, and references therein) which actively respond to sharp features to limit growth of high wavenumber modes. Satisfactory results are achieved because a hydrodynamic calculation only requires a first difference to calculate the pressure gradient acceleration. It is precisely the local adaptability of flux-correcting schemes that violates a tenet of Richardson's hypothesis, and it is perhaps not too surprising to find schemes originally designed for hydrodynamics producing anomalous spikes in *second* differences. Such current reversals are a major problem in attempts to make use of the vector potential in MHD simulations.

The problem of anomalous current reversals produced by the second derivative of the vector potential motivates the alternative approach of direct evolution of the magnetic field components. However, the increased difficulty of assuring constrained evolution, especially in two-dimensional simulations where the vector potential approach is much simpler, leads to justifiable concern regarding the effect of the nonvanishing field divergence. In discussing this problem, Ramshaw (1983) notes that in many calculations a nonzero $\nabla \cdot \mathbf{B}$ is simply tolerated, provided the momentum equation is in nonconservative form. In rejecting this approach, Ramshaw proposes three ways to enforce $\nabla \cdot \mathbf{B} = 0$: (1) use of a vector potential (discussed above), (2) (possible) incorporation of the constraint within the finite-difference equations, and (3) a method Ramshaw develops, termed "divergence-cleaning," that uses an additional scalar function in the induction equation (see Ramshaw 1983 for further details). We have chosen to implement Ramshaw's second suggestion: the direct incorporation of the constraint within the finite-difference equations.

IV. CONSTRAINED TRANSPORT

a) Finite-Difference Notation

We begin with an introduction of our finite-difference notation. We choose coordinates labeled x , y , and z to span three-dimensional space. It is most important to note, however, that *we do not mean to imply that these are Cartesian coordinates*; equation (2.12) holds in arbitrary coordinate systems including those describing locations on a curved manifold; we choose the labels x , y , and z merely to simplify our notation.

We define a *staggered* spatial mesh that allows straightforward second-order spatial differences to be constructed. This provides different centerings for the finite-difference values of the various physical quantities. Cell corners have the discrete locations $(x_i, y_j,$

and z_k); a quantity Q located at a cell corner would be denoted by $Q_{i,j,k}$. The positions of the mesh corners define zone increments given by

$$\Delta x_{i+1/2} = x_{i+1} - x_i, \quad \Delta y_{j+1/2} = y_{j+1} - y_j, \quad \Delta z_{k+1/2} = z_{k+1} - z_k. \quad (4.1)$$

Zone-centered locations are then described, with half-integer subscripts, by $(x_{i+1/2}, y_{j+1/2}, z_{k+1/2})$ with the definitions

$$x_{i+1/2} = \frac{1}{2}(x_{i+1} + x_i), \quad y_{j+1/2} = \frac{1}{2}(y_{j+1} + y_j), \quad z_{k+1/2} = \frac{1}{2}(z_{k+1} + z_k). \quad (4.2)$$

Hence a zone-centered quantity P is denoted by $P_{i+1/2, j+1/2, k+1/2}$. Zone-center locations in turn define zone-center separations

$$\Delta x_i = x_{i+1/2} - x_{i-1/2}, \quad \Delta y_j = y_{j+1/2} - y_{j-1/2}, \quad \Delta z_k = z_{k+1/2} - z_{k-1/2}. \quad (4.3)$$

As indicated by the subscripts they carry, zone increments need not be constant. In many cases it is advantageous to "stretch" the mesh in one or more dimension and, indeed, the discrete locations can vary in time allowing the mesh to "adapt." Note that when the mesh spacings vary, the cell faces, given by constant values of x_i , y_j and z_k , are not exactly centered between zone-center locations. If the grid stretch is too large (in excess of several percent change from zone to zone) the second-order truncation accuracy of the spatial differences will be progressively lost. However, as we show below, the ability to construct a constrained transport scheme is unaffected by grid stretch. This fact guarantees that an adaptive mesh algorithm can be accommodated within the scheme. Figure 1 is a representative mesh depicting two coordinate directions.

Discrete time levels are indicated by a superscript n . The time interval Δt is defined as $\Delta t = t^{n+1} - t^n$, and is typically a function of time as well.

The usual centering of hydrodynamic quantities places density ρ , energy density $\rho\epsilon$, pressure p , and the generalized Lorentz factor W at zone centers and on the integer time levels n . The relativity quantities, the lapse function α , and the spatial metric γ_{ij} , take the same centering. Velocities V^i , V^i_q , momenta S_i and the shift vector β^i are assigned face-centered locations and are considered located at half-integer time levels $n + \frac{1}{2}$ (HSWb). Figure 1 shows the spatial centerings of a number of these quantities as well as the two-dimensional locations of magnetic field components.

b) Finite-Difference Treatment of Magnetic Field and Flux

As we shall see below, the correct placement of the magnetic field components on the staggered spatial mesh is a key aspect in the development of the numerical scheme. Proper time- and space-centered finite-difference equations can be written by assigning these

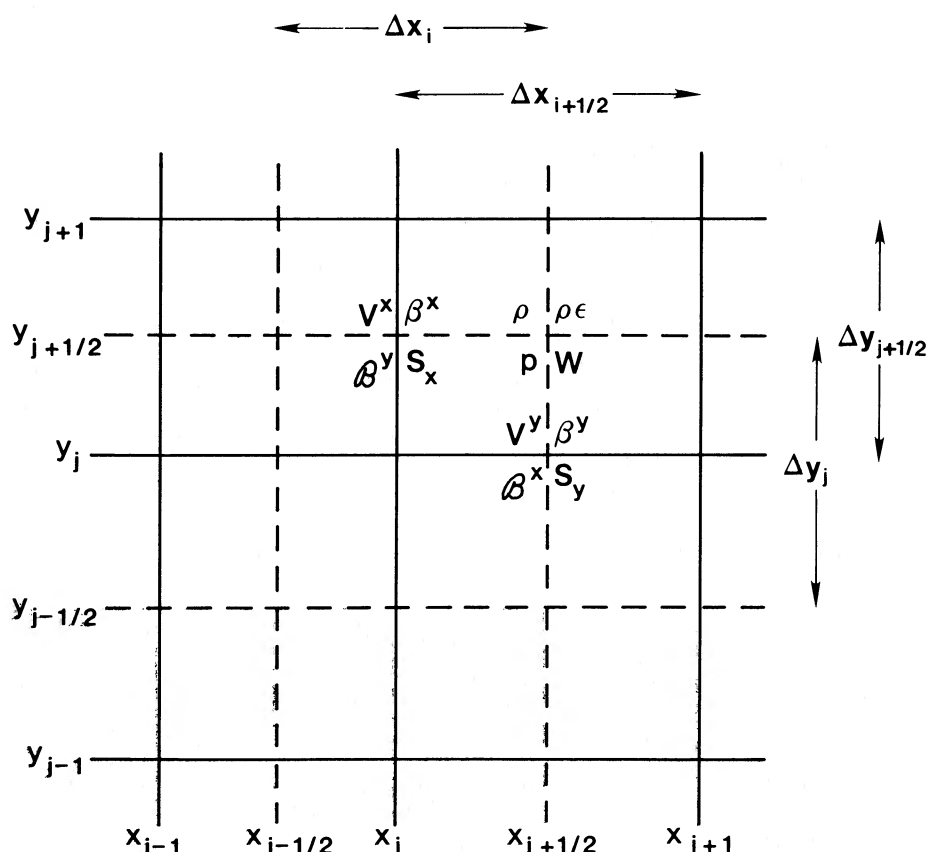


FIG. 1.—A portion of a two-dimensional finite-difference grid. The staggering of the mesh is indicated as is stretch in the mesh. The centering of various physical quantities is also shown.

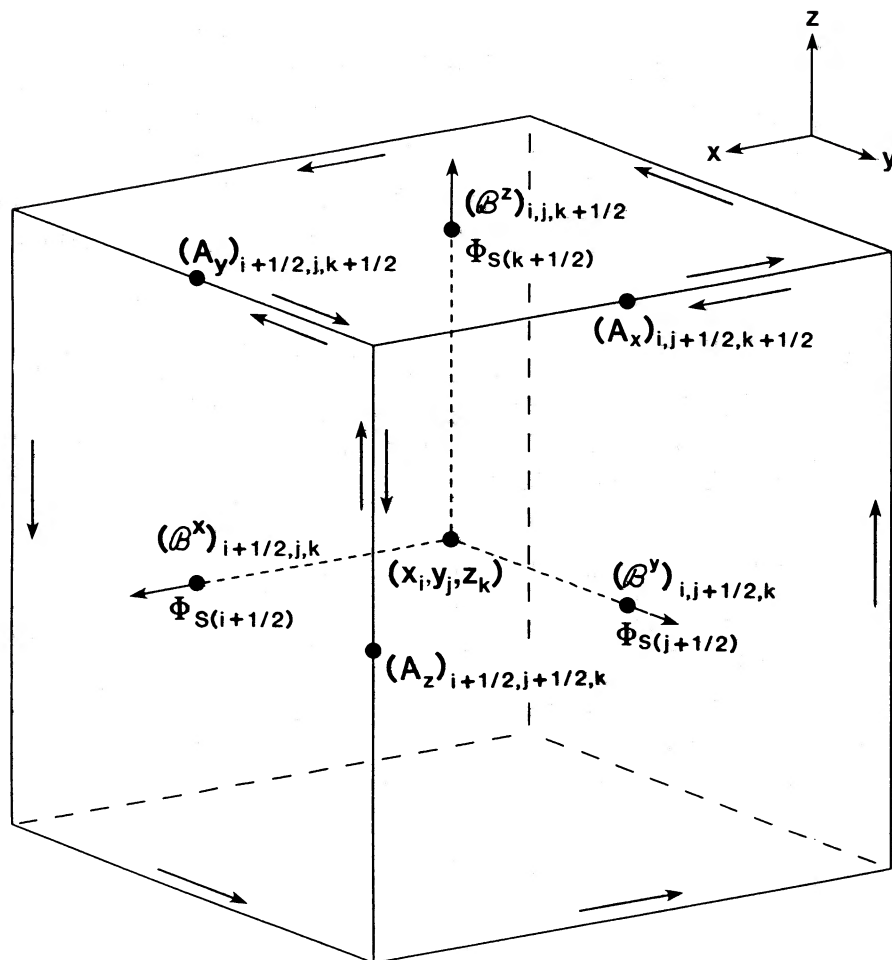


FIG. 2.—The three-dimensional centering of electromagnetic quantities. In the constrained transport scheme the total flux piercing the surface of a finite-difference cell is always zero, achieved by balancing the EMF contributions taken around the cell edges. Arrows indicate the direction of the closed contour integral.

components the centerings (see Fig. 2)

$$(\mathcal{B}^x)_{i+1/2,j,k}^n, \quad (\mathcal{B}^y)_{i,j+1/2,k}^n, \quad (\mathcal{B}^z)_{i,j,k+1/2}^n. \quad (4.4)$$

The magnetic field components are face centered, but in a different way from the velocity and momentum terms.

As mentioned in § II the more fundamental quantity for our purposes is the flux Φ_S piercing a surface S (defined in eq. [2.9]). In equation (2.12) we express the flux as an integral over the magnetic vector density \mathcal{B}^i using the coordinate area element $d\Sigma_i^{(c)}$. This places the integral in a form that can immediately be finite differenced. Take the surface S to be the (staggered) cell face located at the fixed value $x = x_{i+1/2}$ and spanned by zone increments Δy_j and Δz_k . The flux through this face is

$$\Phi_{S(i+1/2)} = \int_{\Delta y_j, \Delta z_k} \mathcal{B}^x dy dz, \quad (4.5)$$

with the orientation chosen so that Φ_S is positive for a positive-directed field component (right-handed rule). We then define the finite-difference value of the \mathcal{B}^x component to be the face area averaged flux

$$(\mathcal{B}^x)_{i+1/2,j,k} = \frac{1}{\Delta y_j \Delta z_k} \Phi_{S(i+1/2)}. \quad (4.6)$$

To see the importance of magnetic flux to the scheme, take the integration over the closed surface $S = \partial\mathcal{V}$ made up of six faces bounding the cell volume \mathcal{V} centered on (i, j, k) as indicated in Figure 2. We know analytically that the net flux through $S = \partial\mathcal{V}$ must vanish so a constraint on our numerical scheme is that

$$\Phi_{S(i+1/2)} - \Phi_{S(i-1/2)} + \Phi_{S(j+1/2)} - \Phi_{S(j-1/2)} + \Phi_{S(k+1/2)} - \Phi_{S(k-1/2)} = 0. \quad (4.7)$$

Since S is a closed surface, we can use Gauss's theorem (in a simply connected region) to write

$$\int_{S=\partial\mathcal{V}} \mathcal{B}^i d\Sigma_i^{(c)} = \int_{S=\partial\mathcal{V}} B^i d\Sigma_i = \int_{\mathcal{V}} \nabla_i B^i d\mathcal{V} = \int_{\mathcal{V}} \partial_i \mathcal{B}^i d^3x = 0. \quad (4.8)$$

We see that the constraint that the total flux through S vanish is connected with a numerical requirement on the finite-difference form of the divergence operator. Substituting the definitions (4.6) into equation (4.7) and dividing by the cell coordinate volume $\Delta x_i \Delta y_j \Delta z_k$ we find

$$\frac{1}{\Delta x_i} [(\mathcal{B}^x)_{i+1/2,j,k} - (\mathcal{B}^x)_{i-1/2,j,k}] + \frac{1}{\Delta y_j} [(\mathcal{B}^y)_{i,j+1/2,k} - (\mathcal{B}^y)_{i,j-1/2,k}] + \frac{1}{\Delta z_k} [(\mathcal{B}^z)_{i,j,k+1/2} - (\mathcal{B}^z)_{i,j,k-1/2}] = 0, \quad (4.9)$$

as the required finite-difference analogue of the divergence constraint on the magnetic field. Between equations (4.7) and (4.9) we have the finite-difference version of Gauss's theorem.

Note that if both the field \mathcal{B}^i and the mesh locations (and zone increments) assume new values during a time step Δt , then a constrained transport scheme must continue to satisfy equation (4.7) with new fluxes related to the new field and zone increment values via equation (4.6).

c) Finite-Difference Analogue of Stoke's Theorem

An important aspect of the CT scheme is the development of a finite-difference analogue of Stoke's theorem. Schnack and Killeen (1980) derive a finite-difference version of Stoke's theorem suitable for general curvilinear coordinates. Here we use this idea to guarantee the vanishing of the divergence of the magnetic field in any coordinate system.

Each finite-difference cell face is bounded by a closed contour made up of four edges. The rate of change per unit coordinate time of the flux through a face is minus the total EMF around this contour; thus

$$\frac{d}{dt} \Phi_{\text{face}} = - \sum_{\text{edges } l=1}^4 \mathcal{E}_l, \quad (4.10)$$

where \mathcal{E}_l are the contributions to the total EMF taken in the sense of a right-handed integration about the bounding contour. There are 12 edges C to each finite-difference cell $V_{i,j,k}$. Edges are associated with constant values of two coordinates; for example the edge $C(i + \frac{1}{2}, j + \frac{1}{2})$ is located at constant values $x = x_{i+1/2}$ and $y = y_{j+1/2}$ and has coordinate length Δz_k . We will define by $\mathcal{F}_{(l)}$ the EMF contributions of the edges with the integrations taken in the increasing coordinate direction. For example the EMF contribution from the edge $C(i + \frac{1}{2}, j + \frac{1}{2})$ is

$$\mathcal{F}_{i+1/2,j+1/2,k} \equiv - \int_{z_{k-1/2}}^{z_{k+1/2}} (u^x \mathcal{B}^y - u^y \mathcal{B}^x) dz, \quad (4.11)$$

where, for simplicity, we have written

$$u^i = V^i - V_g^i - \beta^i, \quad (4.12)$$

for the net velocity.

Assuming for now that the EMF contributions $\mathcal{F}_{(l)}$ are obtained by a suitable finite-difference approximation (to be discussed below), we can obtain from equation (2.12) finite-difference evolution equations for the fluxes:

$$\frac{1}{\Delta t} (\Phi_{S(i+1/2)}^{n+1} - \Phi_{S(i+1/2)}^n) = + \mathcal{F}_{i+1/2,j,k+1/2} - \mathcal{F}_{i+1/2,j,k-1/2} - \mathcal{F}_{i+1/2,j+1/2,k} + \mathcal{F}_{i+1/2,j-1/2,k}, \quad (4.13a)$$

$$\frac{1}{\Delta t} [\Phi_{S(j+1/2)}^{n+1} - \Phi_{S(j+1/2)}^n] = - \mathcal{F}_{i,j+1/2,k+1/2} + \mathcal{F}_{i,j+1/2,k-1/2} + \mathcal{F}_{i+1/2,j+1/2,k} - \mathcal{F}_{i-1/2,j+1/2,k}, \quad (4.13b)$$

$$\frac{1}{\Delta t} (\Phi_{S(k+1/2)}^{n+1} - \Phi_{S(k+1/2)}^n) = - \mathcal{F}_{i+1/2,j,k+1/2} + \mathcal{F}_{i-1/2,j,k+1/2} + \mathcal{F}_{i,j+1/2,k+1/2} - \mathcal{F}_{i,j-1/2,k+1/2}. \quad (4.13c)$$

By accounting for simultaneous changes in the mesh zone increments, these equations are evolution equations for the components of \mathcal{B}^i .

The new total flux through the closed surface of a mesh cell, equation (4.7), found by adding equations (4.13a)–(4.13c) and the similar equations for the faces located at $(i - \frac{1}{2}, j, k)$, $(i, j - \frac{1}{2}, k)$ and $(i, j, k - \frac{1}{2})$, continues to vanish if it did originally, even though the cell position and shape may change. This numerical conservation law follows from the fact that each EMF edge contribution appears in the full sum exactly twice with opposing signs, illustrated in Figure 2 by arrows indicating the directions that the contour integrations follow in computing the changes in equation (4.13).

The fundamental point to recognize is the consistency required. The edge EMF contributions are calculated *once* even though each contribution is used in two separate evolution equations. This is analogous to the more familiar numerical implementation of the continuity equation, where mass conservation is insured by calculating the flux through each face and using it twice, once for mass leaving the volume and once when that mass enters the adjacent volume.

We can use Stoke's theorem and the definition of the vector potential (A11) to relate the fluxes to the line integral over A_k

$$\Phi_S = \oint_{C=\partial S} A_k dx^k. \quad (4.14)$$

This suggests the vector potential components are naturally centered on the same edges as the EMF contributions. We take the centerings

$$(A_x)_{i,j+1/2,k+1/2}, \quad (A_y)_{i+1/2,j,k+1/2}, \quad (A_z)_{i+1/2,j+1/2,k}, \quad (4.15)$$

shown in Figure 2 and the finite-difference definition (for example)

$$(A_x)_{i,j+1/2,k+1/2} \equiv \frac{1}{\Delta x_i} \int_{x_{i-1/2}}^{x_{i+1/2}} A_x dx. \quad (4.16)$$

To obtain a consistent finite-difference expression for the magnetic vector density \mathcal{B}^i in terms of the curl of A_k , divide equation 4.14 by the area of the zone face (eq. [4.6]), and use the definition (4.16). For example, the component \mathcal{B}^x is given by

$$(\mathcal{B}^x)_{i+1/2,j,k} = -\frac{1}{\Delta z_k} [(A_y)_{i+1/2,j,k+1/2} - (A_y)_{i+1/2,j,k-1/2}] + \frac{1}{\Delta y_j} [(A_z)_{i+1/2,j+1/2,k} - (A_z)_{i+1/2,j-1/2,k}]. \quad (4.17)$$

The extensions to the other two components are obvious. This definition produces a magnetic field that is divergence free in a sense that is consistent with the form (4.9) of the divergence operator. Thus the vector potential can be used to specify a properly posed initial magnetic field and can also be incorporated in defining inflow or outflow boundary conditions. As an aside we point out that this analysis provides an approach to the evolution of the vector potential (and hence magnetic field) that satisfies the constraint regardless of the method used to evolve A_i .

It is worth noting here that the CT scheme only guarantees that field evolution *changes* are divergence free. If the initial magnetic field fails to satisfy the constraint, it will continue to do so. A more serious issue arises with inflow and outflow boundary conditions. Here one must be careful to not underspecify or overspecify the field and flow at the boundary. Failure to prescribe free-flow boundary conditions properly can lead to subtle inflow of nondivergence-free magnetic field. Because boundary conditions are frequently changed, we recommend that a global measure of the constraint satisfaction, like the example given in § Vb equation (5.6), be monitored as a diagnostic during simulations.

d) Implementing Constrained Transport

Plasma simulations, in contrast to MHD, involve integrating electron and ion orbits while simultaneously determining the evolution of both the magnetic and electric fields. In such a code, if the electric field components are located on the mesh with the same positions as A_k , then the scheme outlined in the last section would allow magnetic field evolution that maintains the constraint $\nabla \cdot \mathbf{B} = 0$.

In MHD, however, the EMF arises from magnetic field advection, or transport, as the field is dragged along by the conducting fluid. This complicates matters since the numerical treatment of transport operators must deal with the issue of numerical stability. In this section we show how the EMF contributions $\mathcal{F}_{(i)}$ can be computed in a way that maintains stability.

To make the presentation more concrete, and to link with our applications in § V, we now simplify to two-dimensional systems having axisymmetry and assume the use of spherical-polar coordinates (r, θ, ϕ). We let $x \rightarrow r$, $y \rightarrow \theta$, and $z \rightarrow \phi$. With no geometrical terms in the induction equation, these identifications can be made immediately. The only connection with the metric comes when the updated magnetic vector density \mathcal{B}^i is used to give new values of the magnetic induction B^i . With no ϕ -dependence, the component \mathcal{B}^ϕ (the toroidal field) becomes an unconstrained variable. Direct evolution of this field component (Clarke *et al.* 1986) has yielded successfully to numerical treatment in the past. The remaining components, \mathcal{B}^r and \mathcal{B}^θ (the poloidal field), are constrained and thus the focus of our subsequent discussion.

We now reduce down the finite-difference evolution equations (4.13) for the poloidal field components. The only EMF contributions to the evolution of axisymmetric poloidal fields in equation (4.13) are precisely those in equation (4.11) now given by

$$\mathcal{F}_{i+1/2,j+1/2,k} = -\Delta\phi(\bar{u}^r \bar{\mathcal{B}}^\theta - \bar{u}^\theta \bar{\mathcal{B}}^r)_{i+1/2,j+1/2}, \quad (4.18)$$

where bars indicate averages (to be discussed below). The $\Delta\phi$ is arbitrary and is matched by those occurring in the reduction of the expressions (4.6) for the fluxes,

$$\Phi_{S(i+1/2)} = (\mathcal{B}^r)_{i+1/2,j} \Delta\theta_j \Delta\phi, \quad (4.19a)$$

$$\Phi_{S(j+1/2)} = (\mathcal{B}^\theta)_{i,j+1/2} \Delta r_i \Delta\phi. \quad (4.19b)$$

Dividing off the $\Delta\phi$ increment, the evolution equations for the fluxes become

$$(\mathcal{B}^r)_{i+1/2,j}^{n+1} \Delta\theta_j^{n+1} = (\mathcal{B}^r)_{i+1/2,j}^n \Delta\theta_j^n - \Delta t[(\bar{u}^r \bar{\mathcal{B}}^\theta - \bar{u}^\theta \bar{\mathcal{B}}^r)_{i+1/2,j+1/2} - (\bar{u}^r \bar{\mathcal{B}}^\theta - \bar{u}^\theta \bar{\mathcal{B}}^r)_{i+1/2,j-1/2}], \quad (4.20a)$$

$$(\mathcal{B}^\theta)_{i,j+1/2}^{n+1} \Delta r_i^{n+1} = (\mathcal{B}^\theta)_{i,j+1/2}^n \Delta r_i^n + \Delta t[(\bar{u}^r \bar{\mathcal{B}}^\theta - \bar{u}^\theta \bar{\mathcal{B}}^r)_{i+1/2,j+1/2} - (\bar{u}^r \bar{\mathcal{B}}^\theta - \bar{u}^\theta \bar{\mathcal{B}}^r)_{i-1/2,j+1/2}]. \quad (4.20b)$$

After the new mesh locations and zone increments are known, these yield updated values of the field components. Note that the adaptive mesh remap algorithm is constructed in a very specific way in equation (4.20) to maintain divergence-free field. In general, a straightforward differencing of the adaptive mesh equation (2.10) would be disastrous to constraint satisfaction.

The \mathcal{B}^r difference that appears on the right-hand side of equation (4.20a) forms a transport term, requiring upwind differencing for stability; the \mathcal{B}^θ difference in the same equation is a shear term that requires no special treatment. However, the same two terms appear on the right-hand side of equation (4.20b) with their roles reversed. What appears as a shear term in one equation is a transport term in the other. The central conclusion of § IVc is that these terms must be differenced in a consistent manner. Hence upwind differencing is required for each such term. The bar over a \mathcal{B}^i component then indicates upwind averaging in the direction of the velocity component with which it is paired. The averaging of velocity components can be done, as usual, by a direct equal-weight average.

The terms $(\bar{u}^r \bar{\mathcal{B}}^\theta)_{i+1/2,j+1/2}$ and $(\bar{u}^\theta \bar{\mathcal{B}}^r)_{i+1/2,j+1/2}$ are “fluxes” in the finite-difference sense. These can be upwind interpolated by a

variety of methods, e.g., (1) donor cell (not recommended), (2) van Leer monotonicity (HSWb and citations therein), and (3) piecewise parabolic (Colella and Woodward 1984), to name a few. For completeness, we outline the application of van Leer monotonicity to CT. The velocity average is (suppressing momentarily the fixed index $j + \frac{1}{2}$)

$$(\bar{u}^r)_{i+1/2} = \frac{1}{2}[(\bar{u}^r)_i + (\bar{u}^r)_{i+1}] . \quad (4.21)$$

Raw slopes are computed as

$$(\Delta_r \mathcal{B}^\theta)_{i+1/2} = \frac{1}{\Delta r_{i+1/2}} [(\mathcal{B}^\theta)_{i+1} - (\mathcal{B}^\theta)_i] \quad (4.22)$$

and are used to calculate a second-order monotonic distribution of slopes

$$\begin{aligned} (\delta_r \mathcal{B}^\theta)_i &= \frac{2(\Delta_r \mathcal{B}^\theta)_{i+1/2}(\Delta_r \mathcal{B}^\theta)_{i-1/2}}{(\Delta_r \mathcal{B}^\theta)_{i+1/2} + (\Delta_r \mathcal{B}^\theta)_{i-1/2}}, & \text{if } (\Delta_r \mathcal{B}^\theta)_{i+1/2}(\Delta_r \mathcal{B}^\theta)_{i-1/2} > 0, \\ (\delta_r \mathcal{B}^\theta)_i &= 0, & \text{if } (\Delta_r \mathcal{B}^\theta)_{i+1/2}(\Delta_r \mathcal{B}^\theta)_{i-1/2} \leq 0, \end{aligned} \quad (4.23)$$

associated with the same locations as \mathcal{B}^θ . These in turn are used to provide the monotonic interpolations of the magnetic field density (restoring the index $j + \frac{1}{2}$)

$$\begin{aligned} (\bar{\mathcal{B}}^\theta)_{i+1/2, j+1/2} &= (\mathcal{B}^\theta)_{i, j+1/2} + \frac{1}{2}(\delta_r \mathcal{B}^\theta)_{i, j+1/2}[\Delta r_i - \Delta t(\bar{u}^r)_{i+1/2, j+1/2}] \\ &\quad \text{if } (\bar{u}^r)_{i+1/2, j+1/2} > 0, \\ (\bar{\mathcal{B}}^\theta)_{i+1/2, j+1/2} &= (\mathcal{B}^\theta)_{i+1, j+1/2} - \frac{1}{2}(\delta_r \mathcal{B}^\theta)_{i+1, j+1/2}[\Delta r_{i+1} + \Delta t(\bar{u}^r)_{i+1/2, j+1/2}] \\ &\quad \text{if } (\bar{u}^r)_{i+1/2, j+1/2} < 0, \end{aligned} \quad (4.24)$$

that, after multiplication by the averaged velocity (4.21), gives the finite-difference “flux.” The extension to calculate the $(\bar{u}^\theta \bar{\mathcal{B}}^r)_{i+1/2, j+1/2}$ “flux” is obvious, as is the extension to three dimensions.

It can be seen that the CT scheme is not overly restrictive. Freedom still exists to modify the transport algorithm further, if desired. For example, one may wish to incorporate consistent advection (Norman and Winkler 1986). The CT scheme is also extendible to nonideal MHD simulations. If the conductivity is finite, one should include the current density term from equation (A13b) in equation (A14) as part of the electric field, which is then used in the resistive induction equation that is the generalization of equations (2.4), (2.8), and (2.12). Since Stoke’s theorem still applies, properly constrained evolution equations can be written.

Because the evolved field is always divergence free, it is possible to reconstruct the vector potential on each time slice. This can be done, up to an arbitrary constant, by integrating

$$dA_\phi = -\mathcal{B}^\theta dr + \mathcal{B}^r d\theta, \quad (4.25)$$

either by holding r constant and integrating \mathcal{B}^r in angle, or by holding θ constant and integrating \mathcal{B}^θ in radius. We have found in axisymmetry that it is best to take the former course since a well-defined boundary condition exists at $\theta = 0$ and $\theta = \pi$.

Since the magnetic vector density \mathcal{B}^i is related directly to the vector potential (4.17), the CT scheme is related to a particular numerical approach for advecting the vector potential. In effect, we are simply obtaining a monotonic distribution of $\partial_i A_\phi$ rather than of A_ϕ . In this way the first derivative is itself constrained to be monotonic, which means that the subsequent derivative used to calculate the Lorentz force will be better behaved near crucial sharp features in the flow.

V. TEST ADVECTION CALCULATIONS

The advantages of the CT technique can be adequately demonstrated by performing a series of simple advection problems. In this section we discuss the results from a series of Cartesian tests, and tests involving the accretion of magnetic field into a black hole. We make use of an existing, calibrated black hole code (HSWb) to which the magnetic induction equations are added. The constrained transport results are compared with those obtained using versions of the code that evolve the vector potential equation. For spherical coordinates this is

$$\partial_t A_\phi = -V^r \partial_r A_\phi - V^\theta \partial_\theta A_\phi. \quad (5.1)$$

The vector potential codes employ three different transport schemes: second-order monotonicity (van Leer’s scheme), first-order donor cell, and a mixed first- and second-order calculation that uses a weighted average of the Lax-Wendroff and donor cell schemes (the “Wilson scheme”; see HSWb). The CT code uses second-order monotonicity. A brief review of certain properties of these schemes will aid the discussion to be presented below.

In advection we are primarily concerned with two types of numerical error: diffusion and dispersion. Diffusion results from the preferential damping of short-wavelength components in a finite-difference function. The preferential damping of short wavelengths causes initially sharp features to spread out over many grid zones. Diffusion is particularly severe in first-order schemes such as donor cell. Dispersion error results from the advection of different wavelength components at different velocities. This will cause an advected pulse to leave a wake or have a precursor. Since short wavelengths are most strongly affected, schemes with low diffusion often exhibit the most difficulty with dispersion. Dispersion is especially troublesome near discontinuities such as shocks since these tend to excite short-wavelength modes. For this reason, while a pure second or higher order scheme is relatively easy to implement, the results are often not acceptable.

Of the schemes we are testing, first-order donor cell is the most diffusive, so much so that an initial discontinuity will be spread out over many zones. The Wilson scheme, a weighted mix of first-order donor cell and second-order Lax-Wendroff, is much less diffusive, although Lax-Wendroff is almost notorious for dispersion error near discontinuities. The weight term alleviates the main difficulties: in regions of smooth flow, the weight factor favors the second-order component, and near shocks the diffusive first-order component removes most of the ringing, insuring a relatively smooth, albeit lower-order, solution. The monotonic scheme chooses between a first- and second-order approximation at each zone through a particular criterion designed to insure that no new extrema are numerically introduced into the solution (discussed above in § IVd). As discussed in § III, the formal order of the first and second derivatives of a function (e.g., J^i) is determined by two things: the formal order of the numerical scheme used, and the application of a weighting function or monotonicity condition. In particular, “hybrid” first- and second-order schemes, such as the Wilson scheme or van Leer monotonicity, can produce sudden changes in first derivatives since the locally determined weights can change abruptly. This point becomes clear in the Cartesian advection tests.

a) Cartesian Advection

We begin with the relatively simple problem of transporting a square wave along a grid with a constant velocity. Each scheme advects a unit amplitude square wave of magnetic vector density \mathcal{B}^x 50 zones wide a distance of 250 grid zones in the y -direction. The Courant factor is set at one-half. The magnetic vector density in the CT scheme is compared with that obtained from the differenced vector potential, and these fields are used in turn to derive a current.

Figure 3 provides a direct comparison of our results. The dashed lines in Figure 3a represent the ideal square wave. The monotonic scheme used in the CT technique advects the pulse reasonably well; the discontinuity at each end has spread out across 16 grid zones. The monotonic vector potential calculation has a slightly smaller zone spread, but new local maxima and minima have been introduced into the magnetic vector density. These are not new extrema in the vector potential; the appearance of the function A_z is not much different from that derived from the CT solution.

The plot of results from the Wilson scheme demonstrates the drawback of the Lax-Wendroff technique; the presence of a steep discontinuity has generated ringing in the function. There is also asymmetry in the solution, another feature associated with dispersion error. The final plot in the series shows that, as expected, the donor cell solution is dominated by diffusion error.

Figure 3b is the current derived from the magnetic field. The ideal solution is a δ -function (current sheet) at the locations indicated by the dashed lines. Constrained transport produces two peaks with a width determined by numerical diffusion. Both the A_z monotonic and Wilson schemes produce decidedly nonmonotonic currents. Not only are the peaks spread over many zones, J^z oscillates with a rather substantial amplitude in the region between the peaks. The change in sign of the current term is a consequence of the introduction of new local extrema into the first derivative. Donor cell does not generate these new maxima, but again, the solution is extremely diffusive.

Differences in the quality of a monotonic CT solution and that of the monotonic vector potential scheme depend on the nature of the function they are advecting. In the present problem, the magnetic vector density consists of two step functions, while the vector potential is a linear ramp between two constant values. Monotonicity advects such structures differently. Although the magnetic vector density derived from the vector potential has the observed wiggles, the step function at either end of the square pulse is sharper than in the CT solution.

The exact manner in which the first derivative is obtained from A_z is not significant. We compared the face-centered difference for \mathcal{B}^x with the zone-centered magnetic vector density taken directly from the monotonic calculation of $\partial_y A_z$. The two approaches produce fields that are essentially identical.

This advection test demonstrates the real advantage of constrained transport: we avoid taking a second derivative to obtain the current. A scheme such as monotonicity will introduce additional extrema into a finite-difference first derivative; in the second derivative these minor annoyances become variations in the sign of the function. Consider, for example, advecting a magnetic vector density \mathcal{B}^x that is proportional to y within a certain region; this is the same function as the vector potential in the square field pulse problem above. Such a field produces a square pulse of current. Advection of that field by the CT technique produces a current exactly like the monotonic vector potential plot in Figure 3a, i.e., with new extrema introduced into the first derivative. However, since no second derivative is required, we do not get a force term that artificially oscillates in sign. Advecting the same function with the monotonic vector potential code produces spatially narrow oscillations of order unity in the current, a potentially disastrous result.

The donor cell solution illustrates Richardson’s hypothesis: since the underlying finite-difference representation of the function A_z is quite smooth, its derivatives are also smooth and first-order accurate. (In fact, a donor cell implementation of CT is identical to the donor cell vector potential scheme.)

b) Radial Accretion

Next consider a series of problems involving the accretion of magnetic field into a Schwarzschild black hole. Standard Schwarzschild coordinates are employed (Misner, Thorne, and Wheeler 1973, hereafter MTW). In these calculations the outer boundary is at $r = 100M$. We have run the problem on a relatively low resolution 64×64 mesh in axisymmetric spherical polar coordinates with evenly spaced zones in angle from 0 to π , and logarithmically spaced radial zones from the horizon to the outer boundary. For simplicity in this problem we have a very low pressure free-falling gas carrying a field into a Schwarzschild black hole, thus creating a stationary radial field. By giving the gas a small, dynamically unimportant amount of angular momentum we also generate a toroidal field.

The steady state solution is obtained by using the free-fall radial velocity with $V^\theta = 0$. The radial field at the outer boundary is obtained from the vector potential

$$A_\phi = k \sin^2 \theta, \quad (5.2)$$

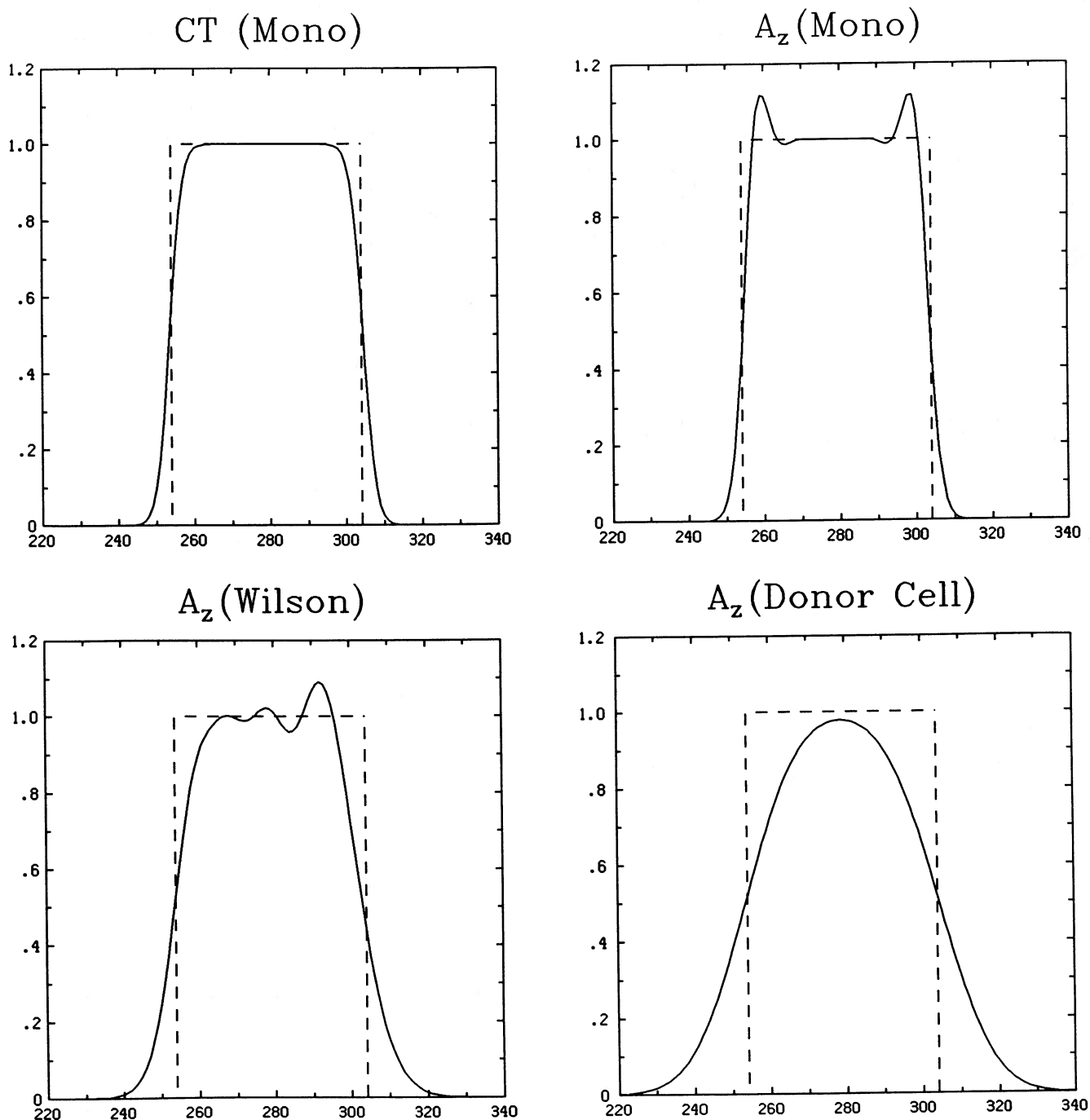


FIG. 3a

FIG. 3.—Results of Cartesian advection test. A square wave of magnetic field is advected by each of the four methods discussed in the text: monotonic constrained transport, monotonic vector potential, Wilson scheme vector potential, and donor cell vector potential. Both (a) magnetic field and (b) current are displayed against the zone number. For the vector potential codes magnetic field is obtained by a finite-difference derivative of A_z and the current by a subsequent derivative. The pulse has been advected a distance of 5 times its width (50 zones wide, initially centered on zone 30). Dashed lines indicate the analytic locations of the edge of the field and the current.

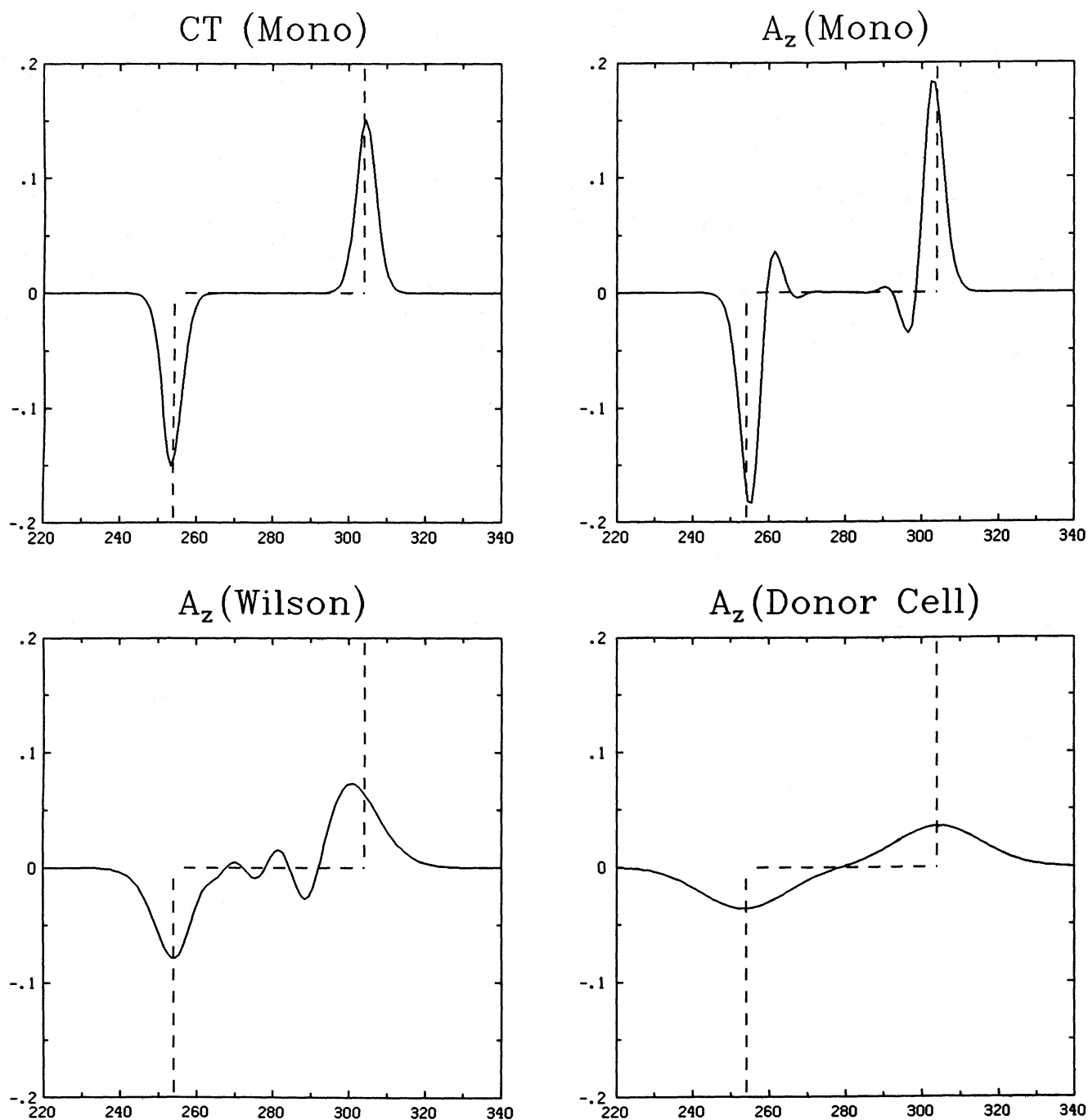


FIG. 3b

where k is some input constant. The angular momentum U_ϕ at the outer boundary is a very small constant l times $\sin^2 \theta$. The steady state magnetic vector densities are

$$\mathcal{B}^r = 2k \cos \theta \sin \theta, \quad (5.3)$$

and

$$\mathcal{B}^\phi = \frac{C(\theta)(r/2M)^{1/2}}{(1 - 2M/r)} - \frac{2kl(r/2M)^{1/2}}{r^2} \sin \theta \cos \theta, \quad (5.4)$$

where the integration constant $C(\theta)$ is determined by setting the toroidal field to zero at the grid outer boundary. For this test the input field and angular momentum constants k and l are set to 10^{-4} .

The constrained transport and the vector potential calculations were run to time $t = 1320M$, or 2.6 free-fall times. During the initial infall, a region of nonzero \mathcal{B}^θ falls from the outer boundary toward the black hole. A direct comparison of the various simulations shows that the monotonic vector potential produces the sharpest pulse, followed by the constrained transport, Wilson, and donor cell codes.

Two free-fall times are required to reach steady state at which time the radial magnetic vector density agrees with the analytic value (eq. [5.3]) to within 0.04% for all calculations. This error is due to the finite-difference term $\Delta \sin^2 \theta / \Delta \theta$. The accuracy could be improved, if desired, through the use of “numerical regularization” (Evans 1986), that is, explicitly taking into account the $\sin^2 \theta$ dependence when formulating the finite-difference operators. The error in the monotonic and donor cell codes is constant with radius while the Wilson scheme vector potential code exhibits long wavelength, small amplitude ($\sim 0.001\%$) variations with radius. This result is consistent with the spherical accretion tests reported on by HSWb.

The toroidal vector density \mathcal{B}^ϕ ranges over three orders of magnitude from the outer boundary to the black hole horizon. Here again, all codes produce very similar results with errors on order 0.5% from near the hole out to $\sim 50M$.

There is one current term in the steady state accretion solution, namely

$$J^\phi = \frac{1}{\sqrt{-g}} \partial_\theta (\sqrt{-g} g^{\phi\phi} g^{\theta\theta} \partial_\theta A_\phi) = \frac{-2k}{r^4}. \quad (5.5)$$

The error in J^ϕ for all codes is 0.004 at all radii. As before, this error is associated with the finite differencing of the $\sin \theta$ terms.

For the CT scheme, we monitor the divergence of \mathcal{B} via the integrated quantity

$$\xi = \left(\sum_{\text{mesh}} |\partial_i \mathcal{B}^i| \right) \left(\sum_{\text{mesh}} \frac{|\bar{\mathcal{B}}^r| + r |\bar{\mathcal{B}}^\theta|}{\Delta r + r \Delta \theta} \right)^{-1}. \quad (5.6)$$

Because of machine roundoff, this quantity does not vanish identically. The error is initially on the order of 10^{-15} . During the course of a simulation this roundoff error accumulates, but at a problem specific rate. By the end of one calculation it had risen to 10^{-10} , while in another (§ Vd) it had reached only 10^{-13} . This accumulation might reach intolerable levels in certain applications. We found that by calculating the evolution of the magnetic vector density components (only) in double precision the error remains on the order of 10^{-15} – 10^{-14} throughout the simulations.

To summarize, all codes perform in a similar manner, giving nearly identical steady state results. Otherwise, the constrained transport and monotonic vector potential codes maintained the sharpest discontinuity during the initial infall, and reached a steady state solution more rapidly than the Wilson and donor cell codes.

c) Infall of a Closed Field Loop

In this test we consider the radial infall of poloidal field loops created by a localized region of toroidal-current-carrying material falling from the outer boundary. By following such an isolated region of field we can further investigate the diffusion and dispersion errors noted in the previous test problems. In addition, this calculation demonstrates the physical process of the destruction of closed field loops by a black hole. Since the field lines are frozen into the fluid, the infall time is just the free-fall time. As before we have compared the constrained transport results with those obtained from the vector potential codes.

The initial conditions are created by allowing a radial flow to carry a field onto the grid (as in the accretion problem above). At $t = 132M$, no further field is sent onto the grid and the field already present is closed off becoming the new initial condition ($t = 0$) for the test. The vector potential code is initialized using A_ϕ obtained from this field. Along an equatorial slice, the vector potential rises from zero, reaches a maximum at the center of the loops, and then declines back to zero. The magnetic vector density \mathcal{B}^θ has, in turn, a “sine-wave” appearance, with a maximum followed by a minimum, and this yields a current with three extrema.

The test is run to time $t = 1053M$ (\sim two free-fall times). Owing to the coarse grid used in these tests, the vector potential profile is poorly resolved (there are only 17 radial zones from the outer boundary down to $r = 35M$.) As in the radial accretion problem described above, the result of this low resolution is rapid diffusion; the two monotonic schemes are the least diffusive, with the monotonic vector potential code producing the sharpest magnetic vector density profiles. This is not surprising since there are more grid zones per wavelength for A_ϕ than there are for the vector density. However, a plot of the current $(-g)^{1/2} j^\phi$ along an equatorial slice at time $t = 132M$ (Fig. 4) again reveals the problem with taking two derivatives of a monotonically advected quantity. Apparently there is one advantage to advecting the vector potential since its characteristic length scale will be larger than for the magnetic vector density. This means that in general the vector potential will be better resolved for a given number of grid zones. Accurate CT calculations may therefore require slightly greater resolution to maintain the same sharpness in the magnetic field. We feel, however, that avoiding oscillations in the sign of the force term more than offsets this cost.

As before, we monitor $\partial_i \mathcal{B}^i$ in the CT method simulation. The error term ξ remains near 10^{-15} .

d) Accretion Disk Formation

We repeat the radial accretion problem described above in § Vb, but raise the value of the angular momentum parameter l to 9 (corresponding to a Keplerian orbit at $77M$). This is a dynamically important value, insuring that much of the infalling gas will pass through strong shocks and form a hot disk orbiting the black hole. This is a low-resolution repeat of a hydrodynamical calculation described in Hawley (1986). There is, of course, no analytic solution available for this problem. The purpose of this test is to check the qualitative performance of the constrained transport code when V^r , V^θ , \mathcal{B}^r , and \mathcal{B}^θ are all nonzero. In particular, we make detailed comparisons of the currents and fields from both the constrained transport and the vector potential calculations.

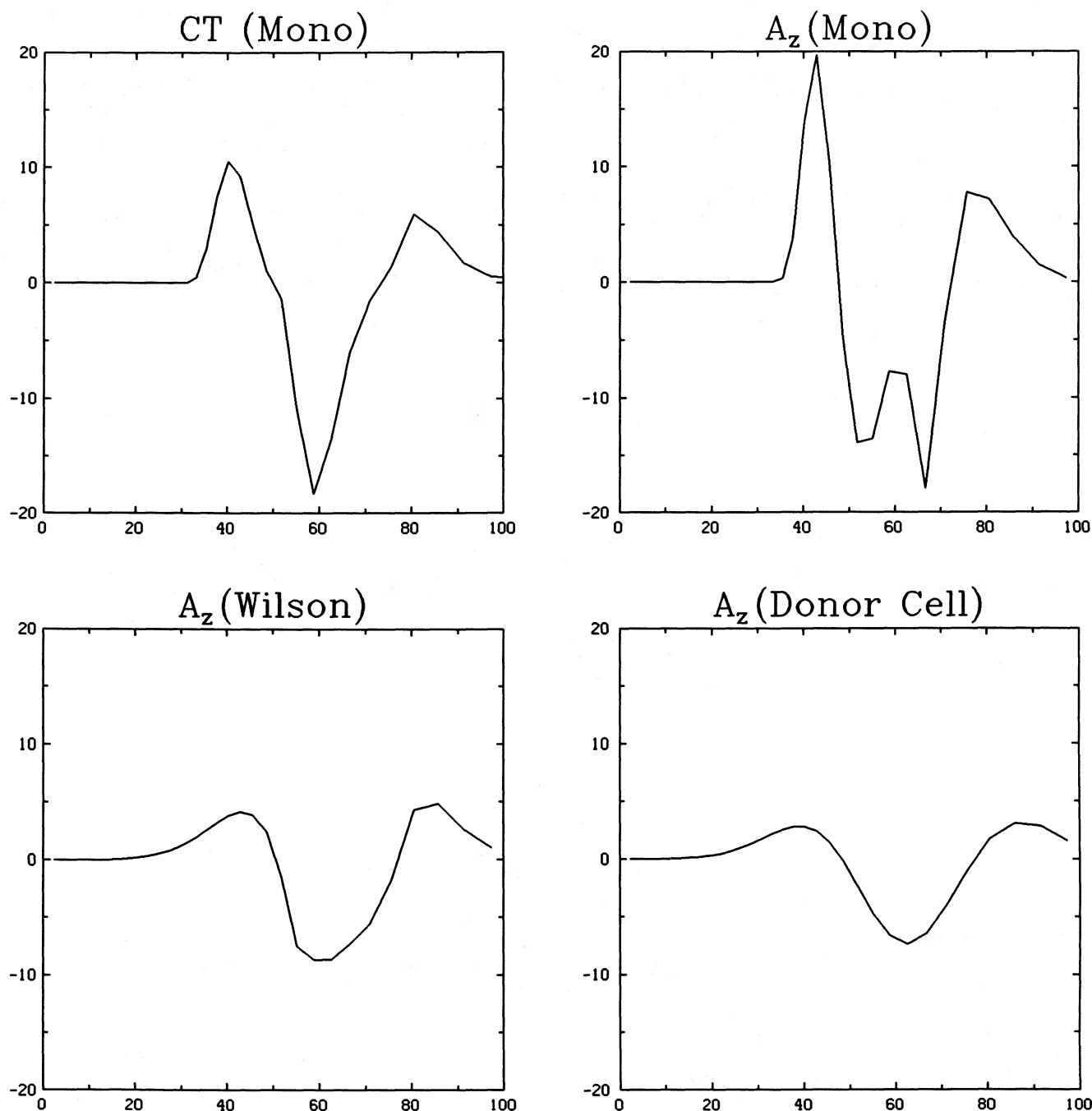


FIG. 4.—Current $(-g)^{1/2} J^\phi$ along the equator at $132M$ for the closed loop infall problem. Qualitatively, the current should rise to a maximum, decline to negative minimum, rise to another positive maximum, and return to zero. In this test, these features must be resolved with only 17 grid zones. The Wilson and donor cell solutions show evidence of substantial diffusion. The monotonic vector potential scheme has the usual anomalous oscillations in the second finite-difference derivative.

Figure 5 shows the derived vector potential in the disk at the end of the CT calculation along with a reference plot of gas density. The plot of A_ϕ from the vector potential code is quite similar. The field lines track the fluid flow pattern: angular momentum diverts the inflowing fluid toward the equator where, during the initial phase of the model, shocks form. The heat generated in these shocks inflates a hot torus orbiting the black hole. Pressure gradient and centrifugal forces drive an outflow along the equator. This in turn bends the field lines back outward.

Comparing derived currents among the various simulations reveals qualitative differences consistent with the features observed in the earlier tests. The constrained transport current is much smoother without being diffusive. Currents derived from two derivatives of the vector potential have additional local extrema on the scale of $2\Delta x$. Although we do not have an exact solution, such local extrema are almost certainly numerical in origin, directly analogous to the results obtained in the Cartesian tests.

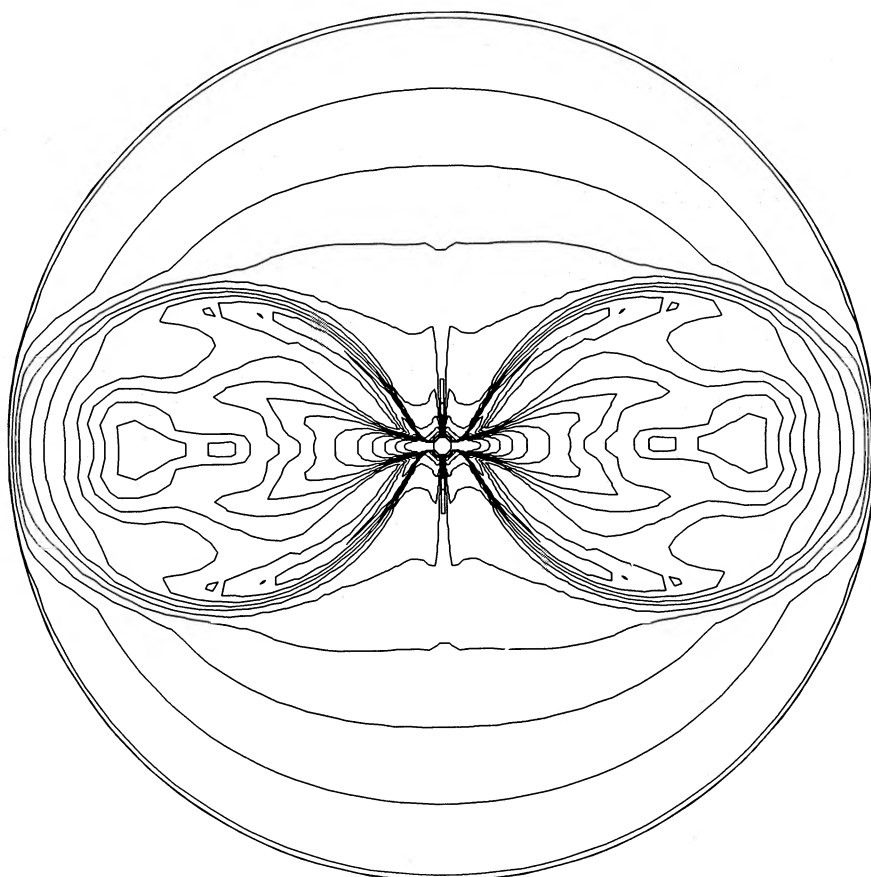


FIG. 5a

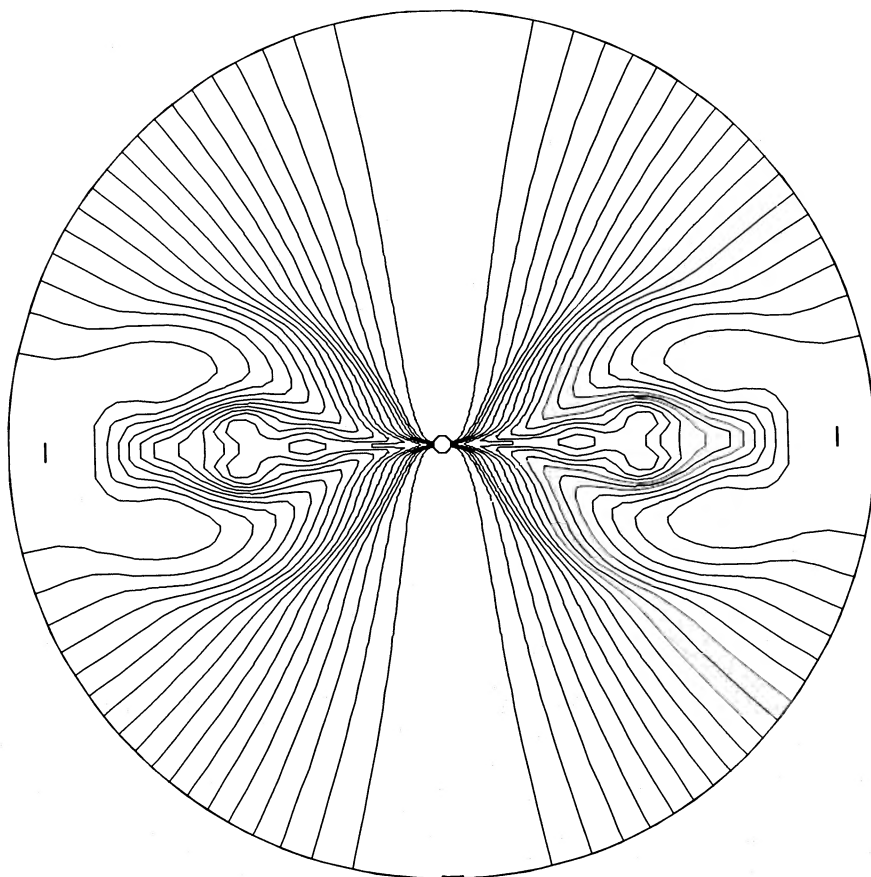


FIG. 5b

FIG. 5.—(a) Logarithmic density contours and (b) vector potential contours for the constrained transport disk formation simulation

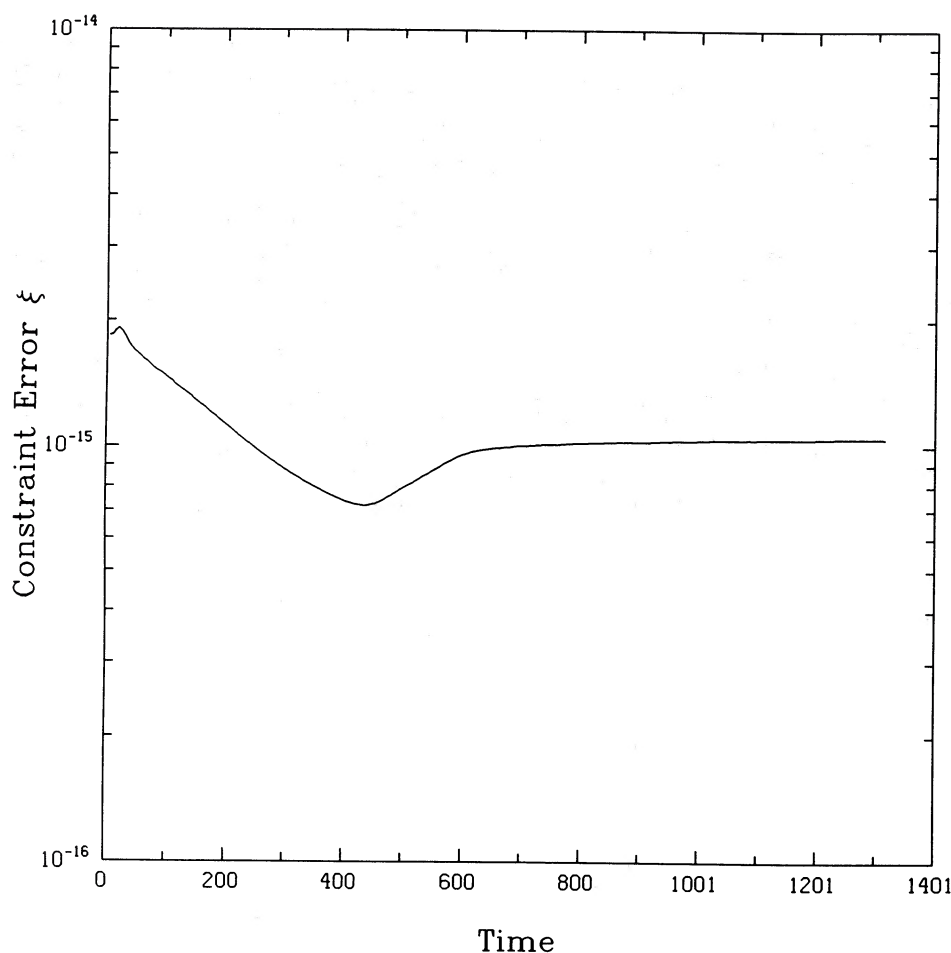


FIG. 6.—Time history of the $\partial_i \mathcal{B}^i$ error term for the constrained transport disk formation simulation

Despite the model's complexity, the field divergence error term ξ remains at the 10^{-15} level. The time evolution of ξ is shown in Figure 6.

VI. CONCLUSIONS

We have developed an approach to the evolution of the MHD induction equation that has the best elements of two previously used techniques, namely, the divergenceless magnetic field associated with the vector potential approach, and currents obtained from a single derivative made possible by the direct evolution of field components. This is accomplished by deriving a simple, general form for the general relativistic MHD induction equation in which the metric does not explicitly appear. Our results are then equally applicable to flat or curved, static or dynamic spacetimes, and in any coordinate system. The induction equation can be placed in an integral form, which in turn leads naturally to a finite-difference equation that, through a finite-difference analogue of Stoke's theorem, manifestly conserves magnetic flux through a closed surface, and hence maintains the constraint equation $\nabla \cdot \mathbf{B} = 0$ to machine roundoff. We call this finite-difference formulation *constrained transport*.

The CT scheme has been tested with several simple advection calculations, both in Cartesian and Schwarzschild coordinates. The tests demonstrate the fundamental advantage of constrained transport: computation of the Lorentz force with the CT scheme requires only one numerical derivative of the function being advected. The second derivatives mandated by a vector potential evolution produce anomalous oscillations in the current; this is a serious difficulty in as much as the amplitude of these oscillations can be comparable with the expected analytic solution. An exception is the first-order vector potential donor cell technique: the solution for the current was smooth, but extremely diffuse. Constrained transport allows higher order schemes to be employed without sacrificing quality in the current.

Our next step will be to complete the MHD code development by investigating finite-difference approaches to the Lorentz force terms. While this is straightforward for the nonrelativistic Lorentz force term $(\mathbf{V} \times \mathbf{B}) \times \mathbf{B}/4\pi$, the additional terms that arise when including full relativity, namely, the displacement current term and finite charge density term, present new numerical challenges. We will analytically explore and numerically test these issues in a subsequent paper.

The authors would like to thank Galen Gisler and John Arons for useful discussions during the ITP "Nanomeeting on Numerical Methods" in 1987 May at the University of California, Santa Barbara. We have also benefited from discussions with K. S. Thorne

and E. S. Phinney on black hole electrodynamics and with M. L. Norman and D. A. Clarke on numerical issues. This work is supported in part by NSF grants PHY83-08826, PHY85-11426, AST86-15325, AST85-14911, and by a Bantrell Fellowship (JFH) at Caltech. Supercomputer calculations were performed on a CRAY X-MP/48 at the NSF National Center for Supercomputer Applications, University of Illinois, Urbana, Illinois.

APPENDIX

MATHEMATICAL DETAILS

I. GENERAL RELATIVISTIC MHD: THE 3 + 1 FORMALISM

The four-dimensional form of Maxwell's equations is not well suited for use in a dynamic numerical simulation. A better approach is to recast the equations into the so-called 3 + 1 form, that (1) explicitly splits apart the time and space dependence, that (2) clearly identifies the dynamical character of the equations, and that (3) gives the general relativistic Maxwell's equations in terms of electric and magnetic field components in a way completely analogous to their usual flat-space presentation. Several recent works on black hole electrodynamics (Thorne and MacDonald 1982; MacDonald and Thorne 1982) and relativistic MHD (Phinney 1983; Sloan and Smarr 1985) have discussed the 3 + 1 formalism. We adhere most closely to the work of Sloan and Smarr (1985), adopting "numerical relativity" notation for the 3 + 1 decomposition of the gravitational field (York 1979; Evans 1984, 1986).

In our notation Greek indices run from 0 to 3 and Latin indices from 1 to 3. Units are assumed such that ($c = 1$) and the metric signature is $(-1, +1, +1, +1)$. We take $g_{\mu\nu}$ to be the spacetime metric and ${}^{(4)}\nabla_\mu$ represents the four-dimensional covariant derivative associated with $g_{\mu\nu}$. Spacetime is decomposed into time slices, each slice labelled by a coordinate time t . Locations on the slice are denoted by spatial coordinates x^i . The unit normal vector field to the slices is n^μ ($n^\mu n_\mu = -1$). The three-metric of the slice is $\gamma_{\mu\nu} = g_{\mu\nu} + n_\mu n_\nu$. The spatial covariant derivative is denoted by ∇_μ . Spatial coordinates x^i are propagated along $t^\mu = \alpha n^\mu + \beta^\mu$, where α and β^μ are the lapse function and shift vector. Thus the line element has the form (2.7). The extrinsic curvature is denoted by K_{ij} , while the acceleration of the surface normals is given by $a_\beta = \nabla_\beta \ln \alpha$. For more details on the decomposition we recommend the excellent review by York (1979).

The Faraday tensor $F^{\mu\nu}$ is decomposed into

$$F^{\mu\nu} = n^\mu E^\nu - n^\nu E^\mu + \epsilon^{\mu\nu\sigma} B_\sigma, \quad (\text{A1})$$

where the electric and magnetic fields satisfy $E^\mu n_\mu = B^\mu n_\mu = 0$ and $\epsilon^{\mu\nu\sigma} = n_\kappa \eta^{\kappa\mu\nu\sigma}$. Similarly, the electromagnetic current four-vector \mathcal{J}^μ is decomposed into

$$\mathcal{J}^\mu = n^\mu \rho_e + J^\mu, \quad (\text{A2})$$

where ρ_e and J^μ are the charge density and (spatial) current density as seen in the frame at rest with respect to the time slice.

Using these to decompose the four-dimensional form of the (general relativistic) Maxwell's equations (see, e.g., MTW 1973), the 3 + 1 form becomes

$$\nabla_i E^i = 4\pi \rho_e, \quad (\text{A3})$$

$$\partial_t E^i = \epsilon^{ijk} \nabla_j (\alpha B_k) - 4\pi \alpha J^i + \alpha K E^i + \mathcal{L}_\beta E^i, \quad (\text{A4})$$

$$\nabla_i B^i = 0, \quad (\text{A5})$$

$$\partial_t B^i = -\epsilon^{ijk} \nabla_j (\alpha E_k) + \alpha K B^i + \mathcal{L}_\beta B^i, \quad (\text{A6})$$

$$\partial_t \rho_e = -\nabla_i (\alpha J^i) + \alpha K \rho_e + \beta^i \nabla_i \rho_e, \quad (\text{A7})$$

where \mathcal{L}_β is the Lie derivative along β^i . The trace, K , is related to changes in the three-determinant $\gamma \equiv \det(\gamma_{ij})$ by (Evans 1984)

$$\alpha K = -\partial_t \ln(\gamma^{1/2}) + \nabla_i \beta^i. \quad (\text{A8})$$

The Lie derivative terms \mathcal{L}_β are transport terms that account for spatial coordinate motion relative to the fiducial observers. For a Schwarzschild background we can take $\beta^i = 0$; for the Kerr metric the nonvanishing gravitomagnetic potential, β^ϕ , plays an important role in the Blandford and Znajek (1977) energy and angular momentum extraction process.

The expression for the Faraday tensor $F_{\alpha\beta}$ in terms of the gradient of the four-vector potential \mathcal{A}_α (see, e.g., MTW 1973) can be decomposed by using

$$\mathcal{A}_\alpha = \phi n_\alpha + A_\alpha, \quad (\text{A9})$$

where A_α is the (spatial) vector potential and ϕ is the electric potential. This then gives

$$\partial_t A_i = -\alpha E_i - \epsilon_{ijk} \beta^j B^k - \nabla_i (\alpha \phi - \beta^k A_k), \quad (\text{A10})$$

$$B^i = \epsilon^{ijk} \nabla_j A_k = \epsilon^{ijk} \partial_j A_k. \quad (\text{A11})$$

Newtonian expressions are recovered by setting $\alpha = 1$ and $\beta^i = 0$.

The (resistive) MHD condition can be written as

$$\mathcal{F}_\mu - \tilde{\rho}_e U_\mu = \sigma F_{\mu\nu} U^\nu, \quad (\text{A12})$$

where σ is the conductivity, $\tilde{\rho}_e$ is the charge density in the *fluid rest frame*, and U^μ is the fluid four-velocity. This can be 3 + 1 decomposed using equation (A2) to yield the two spatial equations

$$W\tilde{\rho}_e = \rho_e - \sigma U^\mu E_\mu, \quad (\text{A13a})$$

$$J_i - \tilde{\rho}_e U_i = \sigma(W E_i + \epsilon_{ijk} U^j B^k), \quad (\text{A13b})$$

where $W = -n_\mu U^\mu = \alpha U^t$ is the generalized Lorentz factor. Using $V^i \equiv U^i/U^t$, the flux-freezing condition ($\sigma \rightarrow \infty$) gives

$$\alpha E_i = -\epsilon_{ijk} V^j B^k. \quad (\text{A14})$$

The Lie derivative term in (A6) when expanded out is

$$\mathcal{L}_\beta B^i = \beta^k \nabla_k B^i - B^k \nabla_k \beta^i. \quad (\text{A15})$$

This can be rewritten in the form of the curl of the cross product of β^i and B^k , which when combined with the K term in equation (A6), using equation (A8), and using the vanishing of the divergence of B^i in equation (A5), gives

$$\alpha K B^i + \mathcal{L}_\beta B^i = \nabla_k (\beta^k B^i - \beta^i B^k) - B^i \partial_t \ln \gamma^{1/2}. \quad (\text{A16})$$

Faraday's law (A6), by using the ideal MHD relation (A14), then becomes

$$\frac{1}{\gamma^{1/2}} \partial_t (\gamma^{1/2} B^i) = \nabla_j [(V^i - \beta^i) B^j - (V^j - \beta^j) B^i]. \quad (\text{A17})$$

The covariant divergence of an antisymmetric tensor has a simple reduction which brings the general relativistic magnetic induction equation (A17) into the final form (2.8).

b) Derivation of Equation (2.12)

The total rate of change of flux through a moving surface is

$$\frac{d\Phi_{S(t)}}{dt} = \frac{d}{dt} \int_{S(t)} B^i d\Sigma_i = \int_{S(t)} (\partial_t B^i d\Sigma_i + B^i \delta_t d\Sigma_i). \quad (\text{A18})$$

We can express the surface area element $d\Sigma_i$ in terms of two coordinates ζ and ξ that span the surface:

$$d\Sigma_i = \epsilon_{ijk} \frac{\partial x^j}{\partial \zeta} \frac{\partial x^k}{\partial \xi} d\zeta d\xi = \gamma^{1/2} [ijk] \frac{\partial x^j}{\partial \zeta} \frac{\partial x^k}{\partial \xi} d\zeta d\xi \equiv \gamma^{1/2} d\Sigma_i^{(c)}, \quad (\text{A19})$$

where $d\Sigma_i^{(c)}$ denotes the coordinate area element. To evaluate the convective derivative of the area element (A19) we assume the coordinates ζ and ξ are fixed with respect to the motion V_g^i of the circuit element, i.e., $\delta_t \zeta = \delta_t \xi = 0$. Then using the definition (2.11) of the velocity of the moving circuit, we have

$$\delta_t \left(\frac{\partial x^j}{\partial \zeta} \right) = \frac{\partial V_g^j}{\partial \zeta} = \frac{\partial V_g^j}{\partial x^i} \frac{\partial x^i}{\partial \zeta}. \quad (\text{A20})$$

We then find the change in the surface area element to be expressed by

$$\delta_t d\Sigma_i = [\partial_t \ln(\gamma^{1/2}) + \nabla_k V_g^k] d\Sigma_i - \frac{\partial V_g^k}{\partial x^i} d\Sigma_k, \quad (\text{A21})$$

which is the surface element (and relativistic) equivalent of the so-called "Euler expansion formula" (Mihalas and Mihalas 1984, p. 58) for volume elements. Combining this with the convective change in B^i (2.10) we have

$$\delta_t B^i d\Sigma_i + B^i \delta_t d\Sigma_i = \frac{1}{\gamma^{1/2}} \partial_t (\gamma^{1/2} B^i) d\Sigma_i + \frac{1}{\gamma^{1/2}} \partial_k (\gamma^{1/2} V_g^k B^i - \gamma^{1/2} V_g^i B^k) d\Sigma_i, \quad (\text{A22})$$

using again the vanishing divergence of B^i . Use of this in equation (A18) yields equation (2.12), the integral form of the field transport equation.

REFERENCES

- Achterberg, A., Blandford, R. D., and Goldreich, P. 1983, *Nature*, **304**, 607.
 Benford, G. 1981, *Ap. J.*, **247**, 792.
 Blandford, R. D., and Payne, D. G. 1982, *M.N.R.A.S.*, **199**, 883.
 Blandford, R. D., and Znajek, R. L. 1977, *M.N.R.A.S.*, **179**, 433.
 Brackbill, J. U., and Barnes, D. C. 1980, *J. Comp. Phys.*, **35**, 426.
 Brecht, S. H. 1985, *Space Sci. Rev.*, **42**, 169.
 Chan, K. L., and Hendriksen, R. N. 1980, *Ap. J.*, **241**, 534.
 Choptuik, M. W. 1986, Ph.D. thesis, University of British Columbia.
 Clarke, D. A., Norman, M. L., and Burns, J. O. 1986, *Ap. J. (Letters)*, **311**, L63.
 Colella, P., and Woodward, P. R. 1984, *J. Comp. Phys.*, **54**, 174.
 Dorfi, E. A. 1986, *Comput. Phys. Comm.*, **43**, 1.
 Evans, C. R. 1984, Ph. D. thesis, University of Texas at Austin.
 ———. 1986, in *Dynamical Spacetimes and Numerical Relativity*, ed. J. Centrella (New York: Cambridge University Press), p. 3.

- Finan, C. H., and Killeen, J. 1981, *Comput. Phys. Comm.*, **24**, 441.
- Hawley, J. F. 1986, in *Radiation Hydrodynamics in Stars and Compact Objects*, ed. D. Mihalas and K.-H. A. Winkler (New York: Springer Verlag), p. 369.
- Hawley, J. F., Smarr, L. L., and Wilson, J. R. 1984a, *Ap. J.*, **277**, 276. (HSWa)
- . 1984b, *Ap. J. Suppl.*, **55**, 211. (HSWb)
- Lind, K. 1986, Ph.D. thesis, California Institute of Technology.
- MacDonald, D. A., and Thorne, K. S. 1982, *M.N.R.A.S.*, **211**, 345.
- Mihalas, D., and Mihalas, B. W. 1984, *Foundations of Radiation Hydrodynamics* (New York: Oxford University Press), p. 58.
- Misner, C., Thorne, K., and Wheeler, J. 1973, *Gravitation* (San Francisco: Freeman) (MTW).
- Norman, M. L., Clarke, D. A., and Burns, J. O. 1987, preprint.
- Norman, M. L., and Winkler, K.-H. A. 1986, in *Astrophysical Radiation Hydrodynamics*, ed. K.-H. A. Winkler and M. L. Norman (Boston: Reidel), p. 187.
- Phinney, E. S. 1983, Ph.D. thesis, Cambridge University.
- Ramshaw, J. D. 1983, *J. Comp. Phys.*, **52**, 592.
- Schnack, D., and Killeen, J. 1980, *J. Comp. Phys.*, **35**, 110.
- Sloan, J., and Smarr, L. L. 1985, in *Numerical Astrophysics*, ed. J. Centrella, J. LeBlanc, and R. Bowers (Boston: Jones and Bartlett).
- Thorne, K. S., and MacDonald, D. A. 1982, *M.N.R.A.S.*, **198**, 339.
- Thorne, K. S., Price, R. H., and MacDonald, D. A. 1986, *Black Holes: The Membrane Paradigm* (New Haven: Yale).
- Wilson, J. R. 1975, *Ann. N.Y. Acad. Sci., Proc. 7th Texas Symposium on Relativistic Astrophysics*, **262**, 123.
- Woodward, P. R., Colella, P. 1984, *J. Comp. Phys.*, **54**, 115.
- York, J. W. 1979, in *Sources of Gravitational Radiation*, ed. L. Smarr (Cambridge: Cambridge University Press), p. 83.

CHARLES R. EVANS: Theoretical Astrophysics, 130-33, California Institute of Technology, Pasadena, CA 91125

JOHN F. HAWLEY: Department of Astronomy, University of Virginia, P.O. Box 3818, Charlottesville, VA 22903